AIChE

Flow Structure Underneath the Large Amplitude Waves of a Vertically Falling Film

Nikolaos A. Malamataris
Dept. of Mechanical Engineering, Technological and Educational Institute of W. Macedonia, GR-50100 Kila, Kozani, Greece

Vemuri Balakotaiah
Dept. of Chemical and Biomolecular Engineering, University of Houston, Houston, TX 77204

DOI 10.1002/aic.11506
Published online May 12, 2008 in Wiley InterScience (www.interscience.wiley.com).

Numerical solutions of the two-dimensional Navier-Stokes equations for vertically falling films show that when the wave amplitude exceeds a certain magnitude, two hyperbolic points on the wall and an elliptic point in the film are generated below the minimum of the wave and travel at the wave velocity. The shear stress along the wall between the hyperbolic points becomes negative and the instantaneous flow field in the film shows roll formation with flow reversal near the wall region. As the wave amplitude increases further, these rolls expand to the free surface dividing the film into regions of up and down flows. For high Kapitza number fluids such as water, multiple regions of up-flow and negative wall shear stress exist with their width oscillating in time. The flow field is interpreted in both stationary and moving frames of reference and in explaining transport enhancements at the wall and free surface. © 2008 American Institute of Chemical Engineers *AIChE J,* 54: 1725–1740, 2008
Keywords: vertically falling film, roll formation, free surface flows, wavy films

Introduction

Free surface flows of thin liquid films along inclined or vertical walls have been studied extensively using laboratory and numerical experiments as well as analytical models. There are many papers and monographs where thorough reviews can be found on the progress made and current understanding of wavy films.[1–8] At present, there are many unresolved issues related to the accurate determination of the streamwise velocity distribution inside the wavy film and the subsequent understanding of the gas to liquid and solid (wall) to liquid heat and mass transfer enhancements. This knowledge is very important, because it leads to accurate calculation of the transfer rates and consequently to a more rational design of equipment where this type of flow takes place. To understand fully how heat and mass transfer are enhanced in a wavy film, the hydrodynamics of this flow must be studied; in particular, the flow field underneath and in the front region of big waves needs to be clarified.

So far, the most established and well understood study of streamwise velocity distributions for this flow has been obtained by Alekseenko et al.,[1,2] who studied liquid films of aqueous glycerin and ethanol solutions at moderate Reynolds numbers ($Re \leq 70$) and Kapitza numbers in the range $100 < Ka < 910$. They concluded that a self-similar parabolic profile describes their experimental data well apart from a narrow region at the minimum film thickness. Because of the scatter of data in that region, there is a lack of knowledge as to how the velocity distributions look like. Alekseenko et al.'s experiments have been performed on film flows where the inlet flow rate was varied periodically (regularly excited waves). They attributed the enhancement of heat and mass transfer to the wavy nature of the film, as they were

Correspondence concerning this article should be addressed to N. A. Malamataris at nmalamat@gmu.edu or V. Balakotaiah at bala@uh.edu.

unable to observe any roll formation or negative velocities in the main hump of the waves or elsewhere.

Wasden and Dukler[9] performed a numerical analysis of naturally excited waves on films of water that have been observed experimentally at large Reynolds number (Re $\geq$ 600, Ka = 4144.5). They concluded that there are regions of large streamwise acceleration in the wave along with regions of circulating flow when viewed in a coordinate system moving with the wave. Miyara[10] also computed a circulation of flow in a moving coordinate system for smaller Reynolds numbers (Re = 100). Many other studies[4,6,11,12] have also shown this region of circulation underneath the hump of a large amplitude wave when viewed in a coordinate system moving with the wave.

The possibility of up-flow near the wall (with negative wall shear stress) in vertically falling films was first conjectured by Massot et al.[13] based on simplified flow models and periodic boundary conditions. Malamataris et al.[14] performed numerical experiments in a wavy film along an inclined wall and computed velocity distributions in the whole area of the computational domain. They found agreement with the generally accepted theory of a self-similar parabolic velocity distribution in most regions of the computational domain. They also found a region of flow reversal in the vicinity of the minimum free surface thickness, which leads to a negative shear stress at the wall. The existence of negative wall shear stress has been confirmed by Tihon et al.[7,15] in laboratory and numerical experiments.

This work is motivated from the need to study the hydrodynamics of vertically falling liquid films with special attention to the flow field in the region underneath and in front of big waves where previous studies showed the existence of a region with negative wall shear stress. The main goal of this work is to elucidate how the flow field in the film evolves as the wave amplitude changes either because of changes in the film flow rate or fluid properties.

This article is organized as follows: the governing equations are presented along with the computational domain, the boundary conditions and the parameters of the flow in the next section. In the following two sections, we present detailed computational results for parameter values that correspond to the experiments of Alekseenko et al.[1,2] and Kapitza and Kapitza.[16] We illustrate new results such as the occurrence of negative streamwise velocity at the free surface and oscillatory roll structures underneath the waves, in these most cited experimental works. We also present a physical interpretation of the computational results in both stationary and moving frames of reference and discuss the influence of the flow field in the film on transport enhancement. In the last section, we summarize the results of this study and discuss some unresolved issues related to falling films.

Governing Equations, Boundary, and Initial Conditions

The computational domain for the vertical wavy film flow is shown in Figure 1. A Newtonian fluid of constant viscosity and density flows in a slit and exits so that it flows along a vertical wall on one side and along a free surface on the other side. The ambient air is considered idle. As shown in

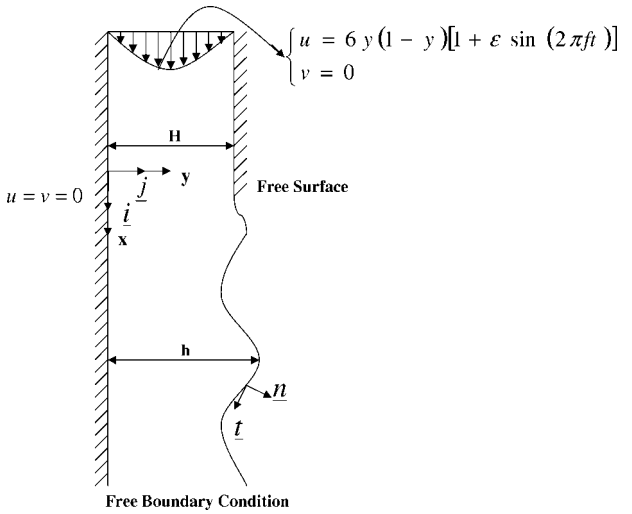

Figure 1. Computational domain and boundary conditions for the wavy film flow along a vertical wall.

prior theoretical studies, the flat film solution is unstable at all flow rates and exhibits *convective instability*, i.e., perturbations introduced at the inlet may grow as they are convected downstream. In the physical or numerical experiments, the perturbations that lead to waves may be introduced in various ways. The flow rate per unit width Γ at the entrance may be varied periodically or suddenly. In this case, the waves are excited in a forced way. If the wall is long enough, waves are induced because of noise in the inlet flow rate or because of ambient pressure fluctuations or because of other disturbances that may enter the film at any streamwise location. In this case, the waves are said to be naturally excited. The waves grow as they travel downstream producing interesting phenomena such as evolution to solitary waves, interfacial turbulence, and spatiotemporal chaos, as discussed in the books by Alekseenko et al.[1] and Chang and Demekhin.[3]

For a two-dimensional isothermal transient flow of an incompressible Newtonian fluid, the dimensionless Navier-Stokes equations are:

$$\nabla \cdot \mathbf{u} = 0 \tag{1}$$

$$\frac{\partial \mathbf{u}}{\partial t} + \mathbf{u} \cdot \nabla \mathbf{u} = -\nabla p + \frac{1}{\mathrm{Re}} \nabla \cdot \left\{ \nabla \mathbf{u} + (\nabla \mathbf{u})^T \right\} + \frac{1}{\mathrm{Fr}} \mathbf{g} \tag{2}$$

The governing equations are given here in their primitive variable formulation. Equations 1 and 2 represent mass and momentum conservation, respectively. Here $\mathbf{u} = (u, v)$ is the dimensionless velocity vector in the fluid, with u and v its components in the x- and y-direction, respectively, and $\mathbf{g}$ is the unit vector in the direction of gravity (in the case of Figure 1, $\mathbf{g} = \mathbf{i}$), p is the dimensionless pressure, $\mathrm{Re} = \rho\Gamma/\mu$ is the Reynolds number with Γ the flow rate per unit span, ρ the density and μ the viscosity of the fluid. (It should be noted that the Reynolds number defined here is one fourth of that used by Mudunuri and Balakotaiah[8]). The group Fr =

U^2/gh_N is the Froude number with g the magnitude of gravity, h_N the Nusselt film thickness, and $U = \Gamma/h_N$ the mean velocity of the flow. Pressure p has been non-dimensionalized with the magnitude ρU^2. Time t has been rendered dimensionless with term h_N/U. Because of the nondimensionalization of the equations with the flow rate Γ and the Nusselt film thickness h_N, the Froude number is related to the Reynolds number Re by Fr = Re/3. The Nusselt film-thickness h_N is given by

$$h_N = \left(\frac{3\mu\Gamma}{\rho g}\right)^{\frac{1}{3}}$$

The boundary conditions for this flow are depicted in Figure 1 and given in equations below:

At the entrance:

$$u = \frac{6}{\gamma^2} y\left(1 - \frac{y}{\gamma}\right)(1 + \varepsilon \sin(2\pi f t)) \tag{3}$$

$$v = 0 \tag{4}$$

Along the walls of the slit:

$$u = 0 \tag{5}$$

$$v = 0 \tag{6}$$

Along the vertical wall:

$$u = 0 \tag{7}$$

$$v = 0 \tag{8}$$

Along the free surface:

$$\mathbf{n}.\mathbf{T}.\mathbf{n} = 2H_c We \tag{9}$$

$$\mathbf{n}.\mathbf{T}.\mathbf{t} = 0 \tag{10}$$

$$v = \frac{\partial h}{\partial t} + u\frac{\partial h}{\partial x} \tag{11}$$

At the outflow: free boundary condition.

Equations 3 and 4 impose a parabolic slit flow at the entrance of the computational domain. The parameter γ is the ratio of the slit width H (see Figure 1) to the Nusselt film thickness h_N. In this work $\gamma = 1$. That is, the width of the slit is taken to have the same magnitude as the Nusselt film thickness while the length of the slit is $3h_N$. However, the choice of the height of the slit, H, is independent of the dimensionless Nusselt film thickness, h_N, and for the sake of a general formulation of this problem, there should be a distinction between these two dimensions. In more conventional formulations of this inlet boundary condition, this distinction is not made and γ is set equal to one.[4]

The flow rate pulsates sinusoidally at the entrance (or at $x = -3h_N$) and in this way, regular periodic waves may be produced depending on the forcing frequency f. The parameter ε is the dimensionless magnitude of forcing with $0 < \varepsilon < 1$. The inclusion of the slit at the entrance of the flow domain is used for the first time for this flow. It has the advantage that relatively high forcing amplitudes ε may be used that reveal the asymptotic wave structure with much shorter domain lengths in the streamwise direction, reducing the computational effort as will be shown later. Malamataris et al.[17,18] used successfully the same approach.

The no-slip boundary condition has been imposed along the walls of the domain (Eqs. 5–8). Normal stress equilibrium is formulated along the free surface with Eq. 9, where $We = \sigma/\rho U^2 h_N$ is the Weber number, with σ the surface tension of the fluid, $2H_c = h_{xx}/(1+h_x^2)^{3/2}$ the mean free surface curvature, and $\mathbf{T} = -p\mathbf{I} + \frac{1}{Re}[\nabla\mathbf{u} + (\nabla\mathbf{u})^T]$ the dimensionless stress tensor of the fluid, with $\mathbf{I}$ the identity tensor. Tangential stress equilibrium is formulated along the free surface with Eq. 10. In Eqs. 9 and 10, the term $\mathbf{n} = (-h_x\mathbf{i} + \mathbf{j}/\sqrt{1+h_x^2})$ is the unit vector normal to the free surface and the term $\mathbf{t} = (\mathbf{i} + h_x\mathbf{j}/\sqrt{1+h_x^2})$ is the unit vector tangential to the free surface, with h the location of the free surface and $h_x = \frac{\partial h}{\partial x}$, as shown in Figure 1 as well. Equation 11 is the (kinematic) condition of no mass penetration across the free surface, which is solved simultaneously with the governing equations to yield the location of the free surface at each point of the computational domain.

The free boundary condition has been applied at the outflow, to let the fluid leave the computational domain freely without any distortion of the flow in the interior. This outflow boundary condition enables waves to exit from the computational domain at any Reynolds number as opposed to other exit boundary conditions which are limited to low Reynolds numbers.[4,5] The free boundary condition has been initially used in free surface flows by Malamataris and Papanastasiou.[17] As discussed by Gao et al.,[4] in other direct numerical calculations[19–21] periodic boundary conditions were used which enforce conservation of mean film thickness and limit the study to single developed waves. In recent direct numerical simulations,[5,22] the study is limited to low Reynolds numbers due to back-flow from the exit, caused by the imposition of other outflow boundary conditions.

The formulation of the problem yields two dimensionless numbers: the Reynolds and the Weber numbers. However, it is more helpful to analyze this problem using the Weber and Kapitza number as shown in the work of Panga and Balakotaiah.[23] The Kapitza number is defined as $Ka = \frac{\sigma}{\rho\nu^{4/3}g^{1/3}}$, with ν the kinematic viscosity of the fluid. Given any Kapitza and Weber number, the Reynolds number may be calculated as $Re = \left(\frac{3^{1/3}Ka}{We}\right)^{3/5}$.

As explained by Panga and Balakotaiah,[23] for free falling vertical films, the magnitude of the Weber number determines the importance of inertial effects and the complexity of the film profile increases with increasing Ka and decreasing We values. Based on the magnitude of the Weber number, the film behavior can be divided into the viscocapillary ($We \geq 1$) and inertial regimes ($We < 1$). All the calculations presented in this work are confined to the viscocapillary regime.

The computational mesh used in this work along with other computational details follow the work of Malamataris et al.[14] and hence will not be repeated here. Table 1 gives information related to the mesh used in the present computations. All results that are presented in the next section are independent of time step and mesh resolution with six decimal

Table 1. Mesh Resolution Used in This Work

Mesh tessellation	x-direction: 10 elements per Nuβelt film thickness y-direction: 10 elements spaced from 0 to h (s. fig. 1)
Length of domain	300 to 1000 Nuβelt film thicknesses
Number of elements	30,300 to 100,300
Number of nodes	133,282 to 421,282
Length of slit	3 Nuβelt film thicknesses
Number of unknowns	293,904 to 972,904
Dimensionless time-step	0.025
CPU per time step	48 to 204 s
Number of time steps for fully developed waves	16,000 to 24,000
Average time for one complete run	5 to 50 days
Computer	Xeon processor at 2.4 GHz, 4 GB RAM

or better accuracy for both pressure and velocities. To determine this independence of results due to discretization, the code was run with a denser mesh and a finer time step by doubling the number of elements in the x- and y-direction and reducing the time step by a factor of 2.

The ultimate criterion for the validity of any computational result is the comparison with available laboratory experimental data. The computed results of this work have been extensively validated against experiments in previous publications of Malamataris et al.[14,17,18] and Tihon et al.[7] However, some additional comparisons with experiments are given in the next section, confirming further the validity of the computed results.

Flow Structure Underneath the Waves in the Experiments of Alekseenko et al.

Alekseenko et al.'s[1,2] and Kapitza and Kapitza's[16] laboratory experiments represent the two most cited experimental results on vertically falling films. In this work, we perform numerical experiments under their process conditions, to provide additional evidence for the accuracy of our computed results. Additionally, we have discovered the existence of negative streamwise velocity all the way up to the free surface and other finer details in the flow field that have not been recognized in prior studies.

Analysis of Velocity Profiles

Alekseenko et al.[1,2] measured velocity distributions in vertically falling thin liquid films. Their aim was twofold: to examine whether the hypothesis of a self-similar parabolic velocity profile is correct for this kind of flow and to investigate if vortices are formed in the film, leading to enhanced heat and mass transfer between the liquid film and the surroundings. They used a water–glycerin solution with a kinematic viscosity $v = 7.2 \cdot 10^{-6}\ m^2/s$, at a Reynolds number of 12.4 and they produced three kinds of waves. However, the magnitude of the forcing frequencies was not reported in their work. The corresponding Kapitza and Weber numbers were 202.27 and 4.39, respectively.

In our work, we reproduced the three types of their waves using dimensionless pulsing frequencies of 0.15, 0.079, and 0.05 with an amplitude of 50% (or $\varepsilon = 0.5$). Figure 2 shows the development of the three waves in a domain that extends 200 dimensionless units downstream the slit exit, while the shape of the single waves is shown in Figure 3. The waves reach their asymptotic shape after about 80 dimensionless units. The dimensionless time in Figure 2 is 200 units. As the frequency of the pulsing decreases, solitary waves of the γ_2 family appear.[3,24] This result has also been confirmed by the experiments of Liu and Gollub[25,26] on inclined film flows.

Table 2 compares the computational results of this work with the measurements of Alekseenko et al.[1] regarding the maximum wave amplitude h_{max}, the wavelength λ, and the wave velocity or celerity Ce. There is excellent agreement in the calculation of the maximum height h_{max} where the deviation is less than 1%. The agreement is also good in the speed of the waves Ce where the deviation is 10.8% for the wave structure of Figure 3c and 6.8% for the wave structure of Figure 3a, while the results for the wave structure of Figure 3b are almost identical. Finally, the agreement is relatively good in the wavelength λ, where the deviation for the wave in Figures 3b, c is 8.4% and 15%, respectively. There is a

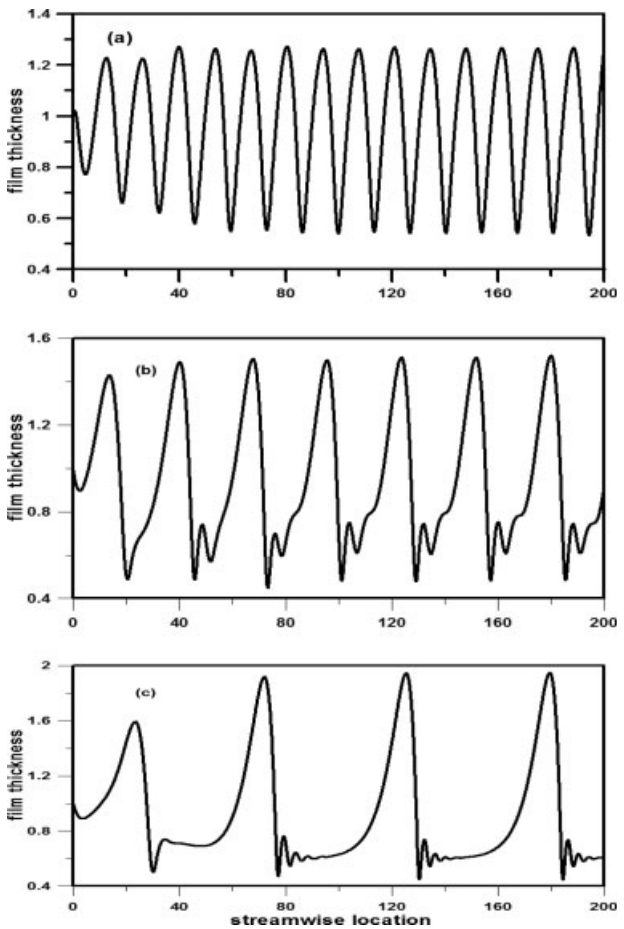

Figure 2. Numerical results for the evolution of waves at Alekseenko et al's experimental conditions.[1]

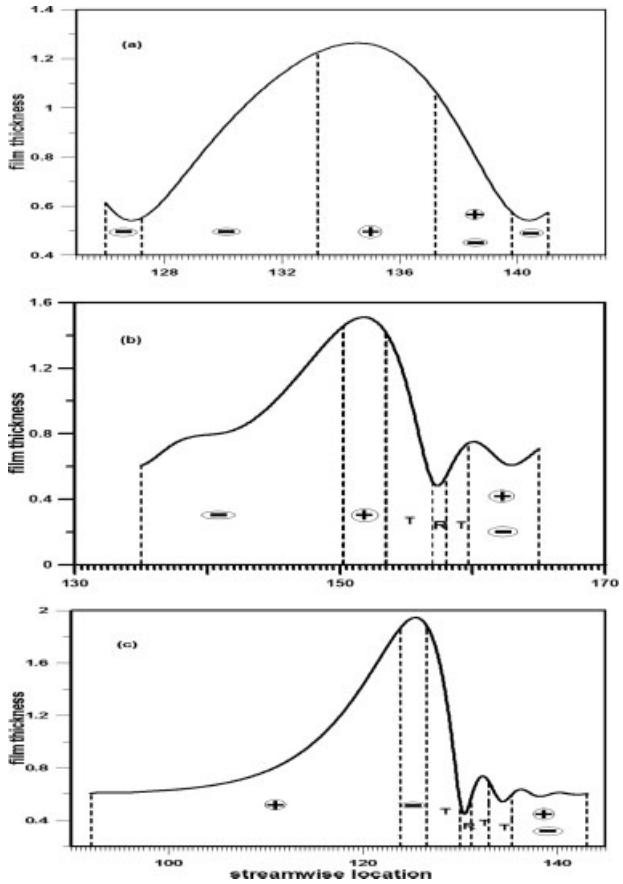

Figure 3. Single waves for the corresponding cases of Figure 2 along with characterization of the regions with respect to the self similar parabolic velocity profile.

large deviation of 53% between the results of this work and Alekseenko et al.'s measurements for the wave in Figure 3a for reasons that are not well understood, since the rest of the comparisons is within the limits of experimental error.

Comparison of the streamwise velocity distributions for the wave in Figure 3a shows a maximum deviation of 33% at $x = 127.2$ (which is at the minimum of the wave) from the self-similar parabolic velocity profile. The deviation is smaller at other locations, e.g., the maximum deviation is 9.8% at $x = 137$. Alekseenko et al.[1] have identified only the region of the self-similar parabolic velocity profile for this wave, along with a region of scatter.

The velocity distributions in the streamwise direction of the wave in Figure 3b are shown in Figure 4. The solid curve is the self-similar parabolic velocity profile. For this wave, the phenomena are more complex and the profiles are shown at some selected locations. In the region $135 \leq x \leq 150.2$ (Figure 3b), the actual velocity profile is less filled than the parabolic profile with a maximum deviation of 17% at $x = 135.5$. [Remark: This terminology is the same as that used by Alekseenko et al.[1] and Malamataris et al.[14] Less (more) filled is indicated by a $\ominus$ ($\oplus$) sign in Figure 3 and implies that the actual u-velocity at any y-location is smaller (larger) than that predicted using self similar parabolic profile assumption]. This profile is shown in Figure 4(i). Then the velocity profile becomes more filled in the region $150.2 < x \leq 153.5$ with a maximum deviation of 14% at $x = 153.5$, which is also shown in Figure 4(i). These two profiles are the bounds within which all actual velocity profiles lie in the region $135 \leq x \leq 153.5$. By inspecting Figure 4(i) at a glance, one may accept that the self-similar velocity profile is a good approximation for this region of the wave, which constitutes 62% of its wave length. The region $153.6 \leq x < 157$ is where the wave amplitude decreases steeply toward the minimum. There, the deviations are very strong and the bounds are shown in Figure 4(ii). The corresponding (transition) region in Figure 3b is denoted with the letter T. The profile at $x = 156.9$ suggests that the flow starts to reverse. Indeed this is the case, as shown in the velocity profiles of Figures 4(iii), (iv).

The flow reversal region is $157 \leq x \leq 158$, which coincides with the minimum of the wave and the region of the biggest scatter, as observed by Alekseenko and coworkers.[1] Eleven different velocity profiles in this region are shown in Figures 4(iii), (iv). It is interesting to note that at $x = 157.3$, which is the wave minimum, the streamwise velocity component is negative up to the free surface. The flow reversal region is denoted with the letter R in Figure 3b. The region $158 \leq x \leq 158.9$ is the transition from the flow reversal to the more familiar parabolic profiles. The deviation to the ideal case is from 81% at $x = 158.1$ to 19.5% at $x = 158.9$. In the rest of the domain, $159.8 \leq x \leq 165$, the actual velocity profiles are close to the self-similar one with a biggest deviation of 12.7% at $x = 161$. For this wave, the measurements of Alekseenko et al.[1] are inconclusive—as also pointed out by Tihon et al.[7]—regarding the details of the velocity profiles, since in their Figure 8.36b just data points are shown without any comments.

Because of the flow reversal that occurs, we studied the pressure and vorticity distribution of this flow both along the

Table 2. Comparison of the Numerical Results of This Work with the Measurements of Alekseenko et al.'s[1] Experiments Regarding the Wave Velocity, c, Wave Length, λ, and Maximum Amplitude, h_{max}, for the Runs in Figure 3

	h_{max} (mm)			λ (mm)			c (mm/s)		
Alekseenko et al.	0.73	0.88	1.12	12	15	36	310	340	460
This work	0.7348	0.8788	1.131	7.84	16.3	31.3	290.2	341.6	415
	H_{max} [-]			λ [-]			c [-]		
This work	1.2637	1.5115	1.9453	13.5	28.15	54.1	1.88	2.225	2.7029

The results of this work are shown both in the units given by Alekseenko et al.[1] and in dimensionless units which is the outcome of the computations.

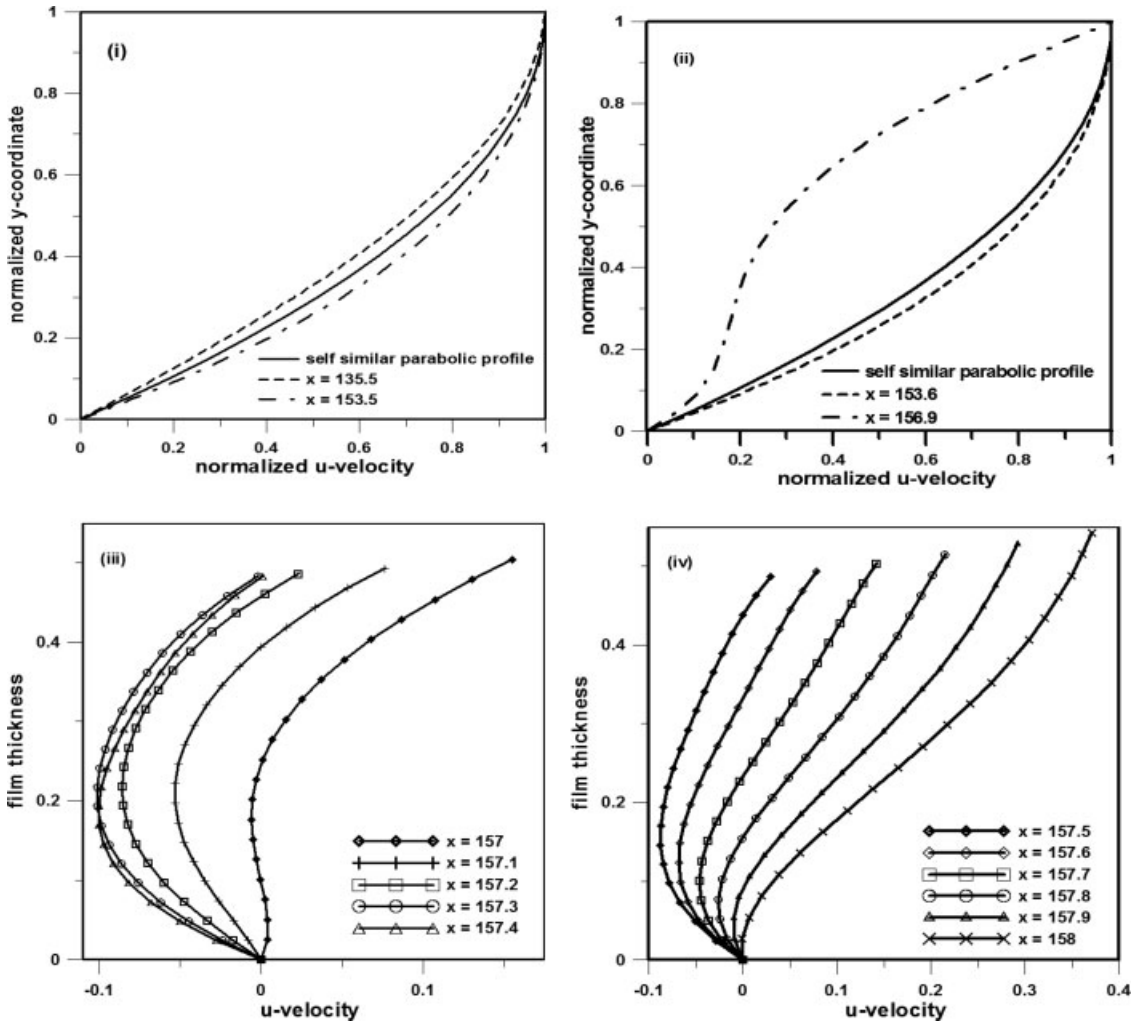

Figure 4. Detailed normalized velocity profiles for the wave in Figure 3b that exhibit the maximum deviation from the self similar parabolic velocity profile along with velocity profiles in the circulation region.

free surface of the wave and along the wall. The vorticity for this case is defined as $\omega = \left(\frac{\partial v}{\partial x} - \frac{\partial u}{\partial y}\right)$. For a flat film, the vorticity is zero at the free surface and decreases monotonically to a value of -3 at the wall while the pressure is constant (at zero) with respect to both x and y. The results are shown in Figure 5. The pressure, both along the free surface and the wall is close to zero up to $x = 151$, which is more or less the region of the wave where the velocity deviations are not big with respect to the self-similar parabolic profile, as shown in Figures 3b and 4. Then, there is a gradual increase in the pressure followed by a rapid decrease. The pressure attains its minimum value at the same x-location as the wave. There is a steep increase in the pressure again followed by a fluctuation of the same manner as the free surface of the wave. The sudden increase in the pressure after the minimum of the wave is the consequence of the flow reversal. It should be noted, that the pressure both along the wall and along the free surface have the same magnitude. Only the minimum value of the pressure is different, which causes a positive pressure gradient in the transverse flow direction at this point. [Remark: The sign changes in the pressure appear to occur at nearly the same location as those in the curvature of the free surface. This is expected based on the normal stress boundary condition].

The vorticity along the free surface is again close to zero up to $x = 153$. It takes a large negative value at the minimum of the wave, due to the fact, that the flow is decelerated there and the streamwise velocity component reaches an even negative value, as shown in Figure 4. Along the wall, the vorticity has a constant negative value (close to -3) in the corresponding part of the flow domain where pressure is constant. Then, due to the flow reversal, the vorticity changes sign and finally, it fluctuates in the same manner as the free surface of the wave and the pressure. It should be noted that since $v(x,0,t) = \frac{\partial v}{\partial x}(x,0,t) = 0$, the dimensionless wall shear stress ($\tau_w = \frac{\partial u}{\partial y}(x,0,t)$) has the same magnitude and opposite sign as vorticity, i.e., in the region of flow reversal, the wall shear stress is negative.

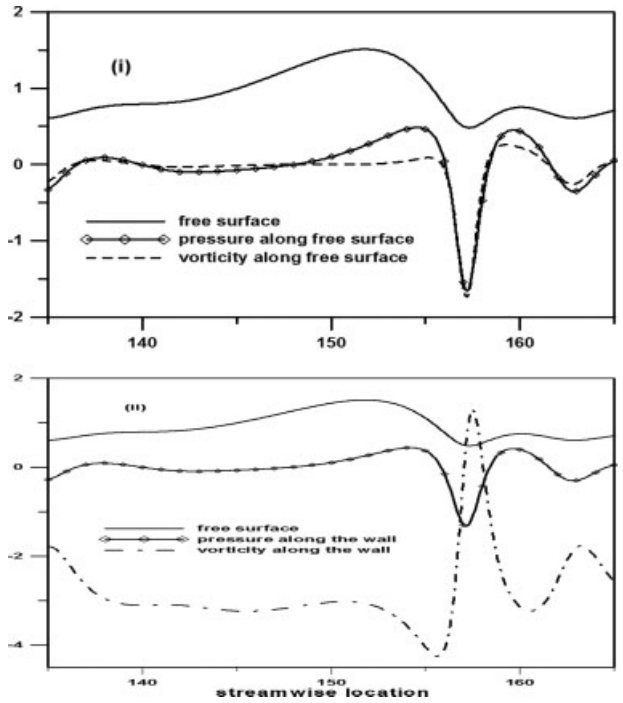

Figure 5. Pressure and vorticity distribution along the wall and the free surface for the wave in Figure 3b.

Another important quantity characterizing the flow reversal is the depth averaged local flow rate $q(x, t)$ defined by

$$q(x,t) = \int_0^{h(x,t)} u(x,y,t)dy \tag{12}$$

Combining the continuity Eq. 1 with the kinematic condition Eqs. 11 and 12 give

$$\frac{\partial h}{\partial t} + \frac{\partial q}{\partial x} = 0. \tag{13}$$

For a wave moving with a constant celerity (Ce), Eq. 13 leads to the following relationship in the traveling wave coordinate ($z = x - \mathrm{Ce}t$):

$$q(z) - \mathrm{Ce}\, h(z) = q_0(\text{constant}) \tag{14}$$

The computed results are shown in Figure 6 for the wave of Figure 3b. The following three important observations can be drawn from this calculation: (i) in the region of flow reversal, $q(x, t)$ attains a negative value, (ii) the region in which the wall shear stress is negative is larger than that in which $q(x, t)$ is negative, and (iii) when the wave form reaches a constant celerity, there is a linear relationship between the local flow rate and film thickness and the slope of this line is the wave celerity. [Remark: Since there are no approximations involved in deriving Eqs. 13 and 14, we can infer that *if the relationship between $q(x, t)$ and $h(x, t)$ is not linear, then the wave shape continues to change and the celerity is not constant*. This observation will be used in the next section in the analysis of Kaptiza's experiment].

It should be pointed out that while negative wall shear stress has been observed in earlier studies of inclined films[7,14] this is the first report of locally negative flow rate in the case of falling films (inclined or vertical). While low-dimensional simplified models[6,8] predict negative wall shear stress, this is the first time a net negative flow rate (and a negative value for streamwise velocity at the free surface) has been calculated for a vertically falling film using the full Navier-Stokes equations. For the calculation in Figure 6, we note that $q_{\min} = -0.03335$ ($h_{\min} = 0.4826$), $q_{\max} = 2.25994$ ($h_{\max} = 1.512$), $q_0 = -1.10890$, and $\mathrm{Ce} = 2.22871$. The physical interpretation of these quantities is given in the next section where the flow fields are interpreted in stationary as well as moving coordinate systems.

The velocity distributions for the wave of Figure 3c are shown in Figure 7. The phenomena in this case are even more complex compared to the previous cases, due to the fact that the wave amplitude is the biggest and the wave minimum is the smallest. The region $92 \leq x \leq 123.8$ is characterized by a less filled parabolic velocity profile with a maximum deviation of 6.34% at $x = 111.1$, as shown in Figure 7(i). By inspecting this figure, one may agree with Alekseenko et al. 's simplification that the profile is indeed self-similar. In the region $123.8 \leq x \leq 126.6$ the profile becomes more filled with a maximum deviation of 28% at $x = 126.6$. This profile is shown in Figure 7(ii) (see also Figure 3c). In the region $126.6 \leq x < 130$ the

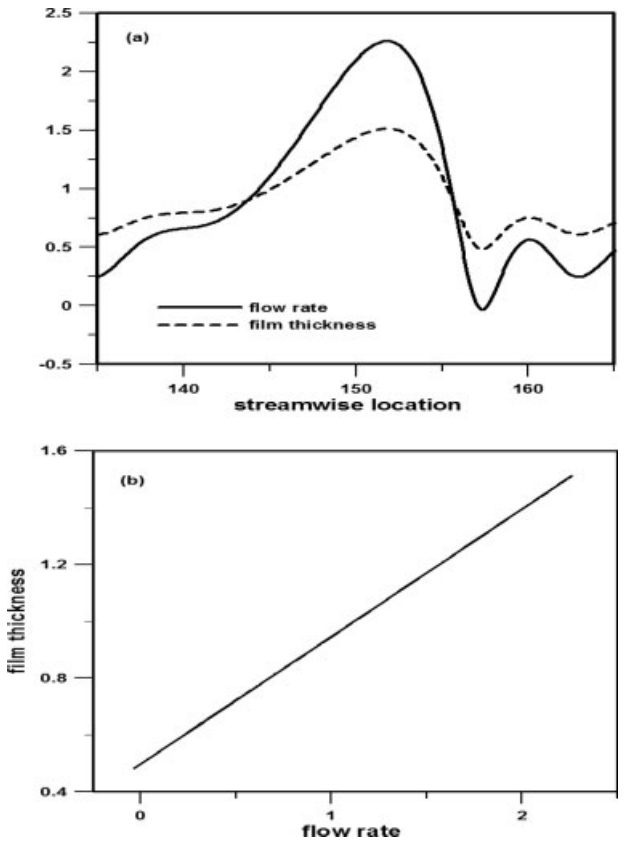

Figure 6. Variation of the flow rate in streamwise direction and observation of linear dependence between flow rate and film thickness for the wave structure of Figure 3b.

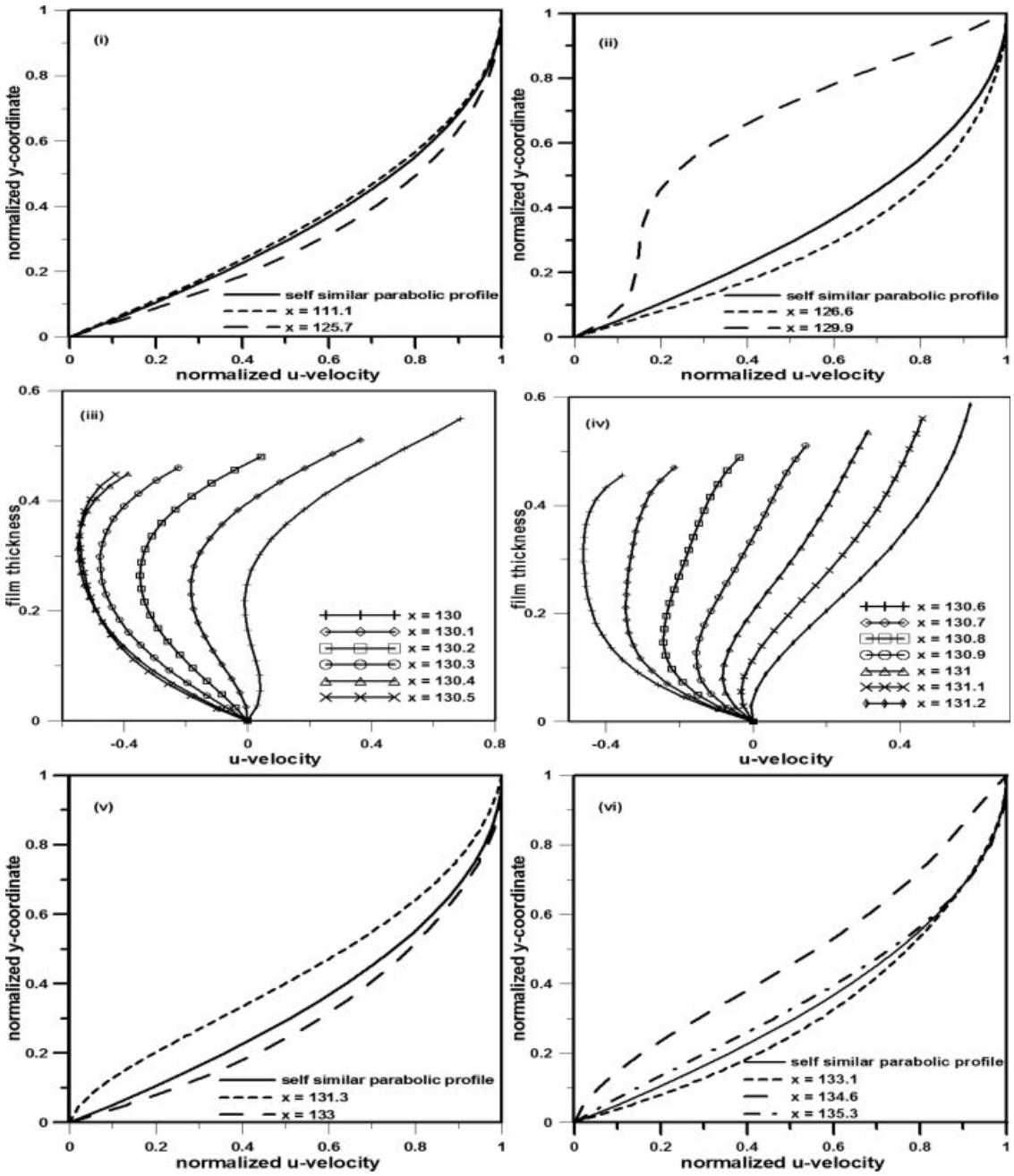

Figure 7. Detailed normalized velocity profiles for the wave in Figure 3c that exhibit the maximum deviation from the self similar parabolic velocity profile along with velocity profiles in the recirculation region.

flow undergoes again a transition to flow reversal where the profile at $x = 126.6$ develops to the profile at $x = 129.9$ in a continuous way as shown in Figure 7(ii). This region is denoted with letter T in Figure 3c. The actual region of flow reversal is at $130 \leq x \leq 131.2$. This region is denoted with the letter R in Figure 3c. The profiles of the streamwise velocities are shown in Figures 7(iii) and (iv). As expected, flow reversal is much stronger here than in the previous case, which is demonstrated by the smaller minima of the velocity and the greater number of locations where the surface velocity is negative ($130.4 \leq x \leq 130.8$).

A transition region follows after the flow reversal which may be divided into two intervals from $131.2 \leq x \leq 133$ and from $133 \leq x \leq 135.3$, which are shown in Figures 7(v) and (vi). These two intervals are denoted with letter T in Figure 3c. In the first interval, the velocity profile deviates between 75.8% at $x = 131.3$ and 34.5% at $x = 133$. In the second interval, the deviation is from 34% at $x = 133.1$ to 78.4% at $x = 134.6$ and finally to 28.3% at $x = 135.3$. In the rest of the domain, that is in the region $134.6 \leq x \leq 141$, the velocity profile has a maximum deviation of 15% at location $x = 137$. The profiles in that region are very close to the self-sim-

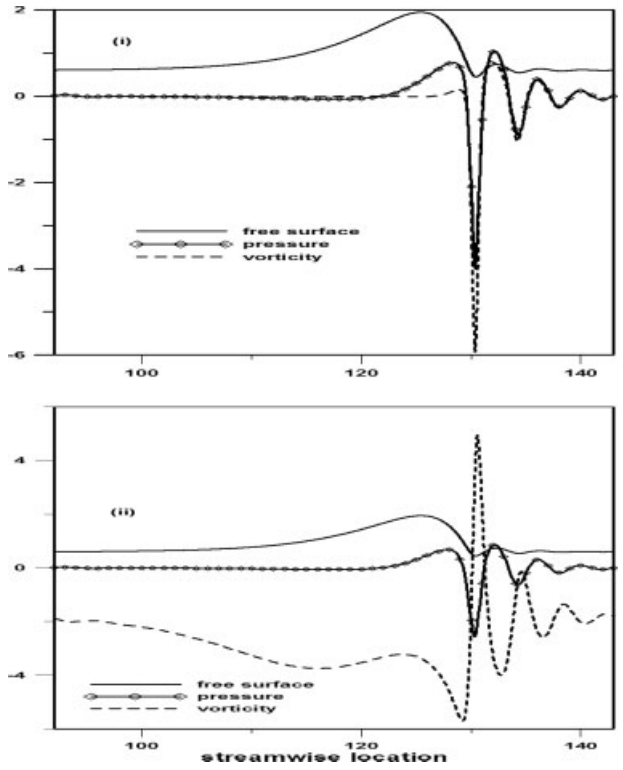

Figure 8. Pressure and vorticity distribution along the wall and the free surface for the wave in Figure 3c.

ilar parabolic one, as was deduced by the measurements of Alekseenko and coworkers.[2]

Figure 8 shows the distributions of pressure and vorticity along the free surface and the wall for this case. The behavior of both magnitudes is analogous to the previous wave. The local flow rate and film thickness profile plots are similar to Figure 6, the only difference is that the extrema of pressure, vorticity, local flow rate, and wall shear stress (which is the negative of the vorticity at the wall shown in Figure 8b) attain greater values, since this wave has a greater amplitude and a smaller minimum than the previous one (for example, $q_{\min} = -0.192253$, $h_{\min} = 0.4476$, $q_{\max} = 3.849068$, $h_{\max} = 1.9447$, $q_0 = -1.40039$, and Ce = 2.69940).

By summarizing the comparison of our calculations with the experiments of Alekseenko et al., we agree quantitatively with almost all of their data apart from one instance of disagreement regarding the magnitude of one wave length. We also agree qualitatively with the fact that the region of the biggest changes in the wave are located in the region of the minimum. However, the computational results shed more light in the vicinity of the wave minimum, which has been termed the region of scatter by Alekseenko et al. and has been poorly understood so far. We found flow reversal and transition intervals upstream and downstream the wave minimum where the deviation of the velocity profiles from the self-similar parabolic one is greater than 15%. Additionally, since the velocity profiles in Figures 4 and 7 exhibit two extrema [$x = 157.1$ in Figure 4(iii) and $x = 130$ in Figure 7(iii)], they can only be described by a cubic or higher order polynomial in y.

Instantaneous Flow Field Structure

The study of the flow field structure is important in understanding the phenomena that take place inside the liquid film. So far, the conventional approach was to solve the Navier-Stokes equations for the vertical film with the Eulerian description and study the streamlines in a reference frame that is moving with the speed of the wave. This approach is used by many researchers in this field.[4–6,9] By studying streamlines in this reference frame that moves with the wave, the appearance of circulation at the main hump of the wave is often interpreted as the reason for enhancement of heat and mass transfer at the gas–liquid interface. However, this circulation is not seen in the laboratory (stationary) frame of reference and, as pointed out by Alekseenko et al.[1] may not be the only reason for enhancement of heat and mass transfer in the film. We discuss here the structure of the flow field in both the stationary and moving reference frames and the physical interpretation of both view points in terms of transport enhancement at both interfaces (gas–liquid and solid–liquid).

First, we note that the stationary view point is not used in the falling film literature but has been in wide use in describing other time varying flow fields such as those in the case of Poiseuille-Bénard convection [s. Xu and Lin[27] and the references cited there]. The local direction of flow in the flat film (up or down) is best understood in the stationary frame of reference. For small amplitude waves (e.g., $h_{\max}/h_N < 1.2$), the wave velocity always exceeds the highest streamwise velocity in the film (at the crest of the wave) and an observer moving with the wave sees no circulation. For large amplitude waves ($h_{\max}/h_N > 1.6$), where the streamwise velocity at the wave crest exceeds that of the wave and the transverse or v-velocity within (one wavelength of) the film changes sign, a circulation can be seen in a reference frame moving with the wave. Assuming that the self-similar parabolic velocity profile is valid near the main hump of the wave, the stream function, ψ, in a coordinate system moving with the wave, may be approximated as

$$\psi = \frac{3q}{h^3}\left(h\frac{y^2}{2} - \frac{y^3}{6}\right) - \mathrm{Ce}\, y.$$

The condition for the appearance of circulation is obtained by setting, $\partial\psi/\partial y = 0$ at $y = h_{\max}$, leading to Ce $h_{\max} + 3q_0 = 0$, or a sufficient condition for circulation is Ce $h_{\max} + 3q_0 > 0$. This condition is barely satisfied for the wave in Figure 3b but is certainly satisfied for that in Figure 3c. Thus, a very small circulation may be seen near the hump in case 3b and a much larger circulation in case 3c. This is confirmed in Figure 9 where we have shown the instantaneous streamlines for the two flows in the moving reference frame. We note that the appearance of a circulation in a reference frame moving with the wave does not imply that the fluid particles trace closed paths in the physical film. However, it implies that the fluid particles that are within the circulation region are indeed trapped in the laboratory frame (or physical film). This trapping can be seen by following the *pathlines* of the fluid

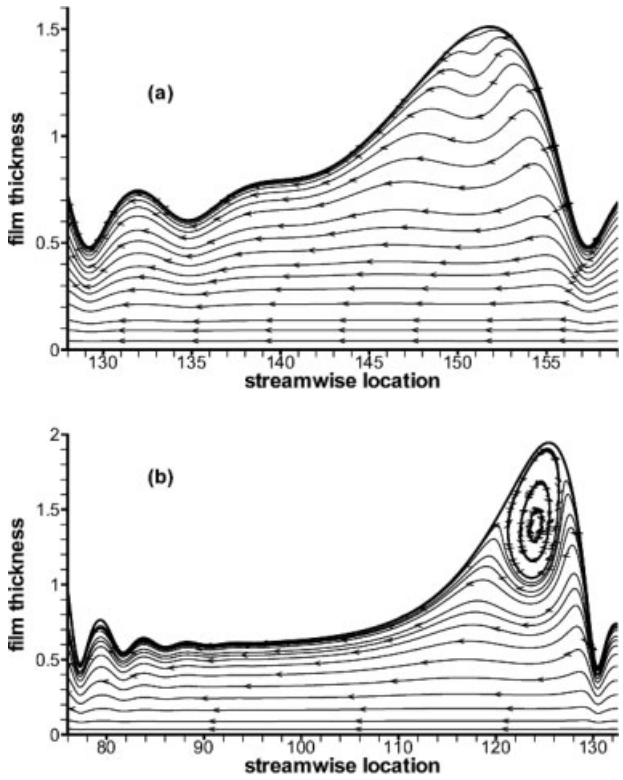

Figure 9. Instantaneous streamlines for the waves in Figure 3b and 3c, calculated at a frame of reference traveling with the speed of the wave.

particles near the main hump. Once the flow field is known, the pathlines are obtained by integrating the equations

$$\frac{dx}{dt} = u(x, y, t), \quad \frac{dy}{dt} = v(x, y, t); \quad (x, y) = (x_0, y_0)|_{t=t_0}$$

where (x_0, y_0) represents any point (fluid particle) in the film.

Figure 10a shows two computed pathlines for the case of waves in Figure 3c. The particle path with starting position (72, 1.34) lies in the circulation region of the wave in Figure 3c and the particle path with starting position (72, 0.77) lies below the circulation region. The particle that lies in the circulation region is confined in the y- direction between the values of 1.15 and 1.65, while the other particle path goes under the minimum of the wave. Figure 10b shows a detail of this particle path when it goes under the minimum where the pathline becomes a cycloid, due to the flow reversal.

We note that a particle is trapped only if the particle transit (or residence) time over a given length L is equal to that of the wave. In dimensionless units, this is equal to L/Ce. Thus, for the wave in Figure 3c with Ce = 2.7029, the transit time from $x = 72$ to $x = 195$ is 45.51 (The region $x = 195$ to $x = 200$ is not used in the calculations in order to exclude exit boundary effects). The computed results for the particles in the circulation region of Figure 3c show that this is indeed the case, as depicted in Figure 10a while the residence time for all other particles is much longer.

In the physical film, a trapped particle accelerates and decelerates both in the x and y directions as it moves in different parts of the wave but does not trace a closed path. However, for an observer moving with the wave, the same particle path appears to trace a closed streamline. We also note that whenever circulation is seen in the main hump in the moving reference frame, the flow field within one wave length shows two hyperbolic points on the surface and one elliptic point in the interior. Further, the observer moving with the wave sees a constant and negative up-flow $q_0 = -1.1089$ for case 3b and $q_0 = -1.40039$ for case 3c everywhere in the film and stationary circulations near the humps.

Figure 11 shows the instantaneous flow field in the stationary frame of reference for the three waves of Figure 3. Here, a stationary observer sees a positive (but varying) flow rate at locations of the wave in case 3a but flow reversal for the waves in cases 3b, c. The flow reversal region is confined in the minimum of the wave, as already discussed in the previous subsection. The instantaneous flow field in this region exhibits roll formation. These roll-type structures possess two hyperbolic points on the wall along with a source and a sink point at the free surface, as will be discussed in more detail later in connection with Figure 13. The local flow rate $q(x, t)$

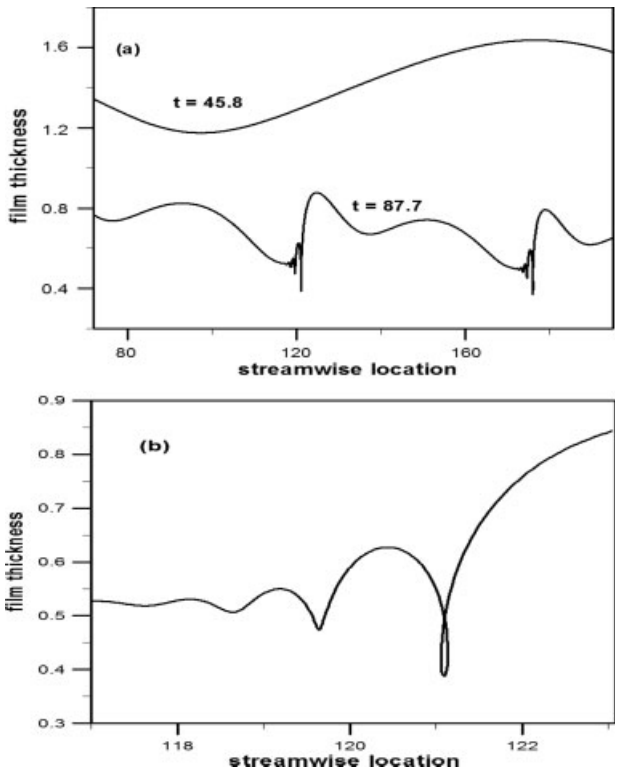

Figure 10. (a) Pathlines of particles with starting positions (72, 1.34) and (72, 0.77).

t is the residence time for each particle until it reaches the outflow. (b) Detail of the pathline of particle with starting position (72, 0.77) indicating tha cycloid type path that this fluid particle undergoes when it flows under the minimum of the wave.

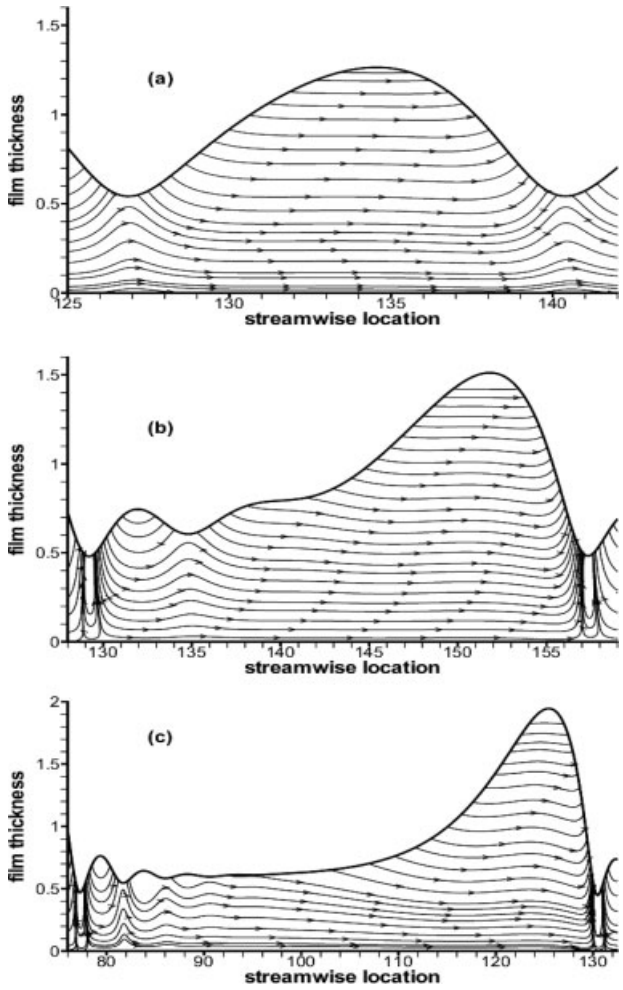

Figure 11. Instantaneous streamlines for the waves in Figure 3, calculated at a frame of reference fixed at the wall (Eulerian approach).

in these regions of flow reversal is negative and the entire film is divided into regions of up (negative) and down (positive) flows. The instantaneous streamlines in this case show cellular structures similar to those observed in Benard or Poiseuille-Benard convection. These cellular patterns correspond to regions of up and down flows in the film.

We note that the hyperbolic points on the wall move with the same velocity as the wave. This implies that each passing wave sweeps the wall and the near wall region with flow reversal. This can also be seen from the pathline shown in Figure 10b, which has cycloid type loops indicating that the fluid particles near the wall region indeed move backward. Thus, the transport enhancement at the wall-fluid interface and the finer details of the flow field near the wall can be seen better in the stationary frame of reference. While the two interpretations are complementary, in our opinion, the stationary interpretation relates to the important physical quantities such as the local flow rate and wall shear stress more directly. For example, if we use the self-similar parabolic velocity profile as a first approximation, the wall shear stress $\tau_w(x, t)$ and the local flow rate $q(x, t)$ are related by

$$\tau_w(x,t) = \frac{3q(x,t)}{h(x,t)^2}$$

Thus, the region of negative wall shear stress and negative flow rate coincide in this first approximation (but as stated earlier, the former region is always larger than the latter without this approximation).

It should be also noted that the pathlines in Figure 10 and the instantaneous streamlines of Figure 11 are consistent, since the streamlines in Figure 11 close to the crest of the wave are more or less parallel to the wall and the streamlines below the crest are curved. As a consequence, it is expected that the particles near the crest are confined in the upper region of the film, as shown in Figure 10a where the particle path in confined in the region $1.15 < y < 1.65$, and the particles away from the crest may move very close to the wall, go below the minimum of the wave and then move away from the wall up to a certain height in the film, as also shown in Figure 10. It should be also noted that the particle paths in Figure 10 are representative for the pathlines of all fluid particles of the waves in Figures 3b and c.

The formation of cellular patterns in the instantaneous flow field of the film intrigued us to compute cases at different forcing frequencies, to understand better how the streamlines evolve underneath the crest of the wave and how roll formation develops as already noted in Figures 11b, c. We picked forcing frequencies of 0.2, and 0.1 and plotted the instantaneous streamlines for the fully developed waves in Figure 12. The dimensionless frequency of 0.2 is greater than the forcing frequency for the wave in Figure 11a and helps us to understand the evolution of the phenomena below

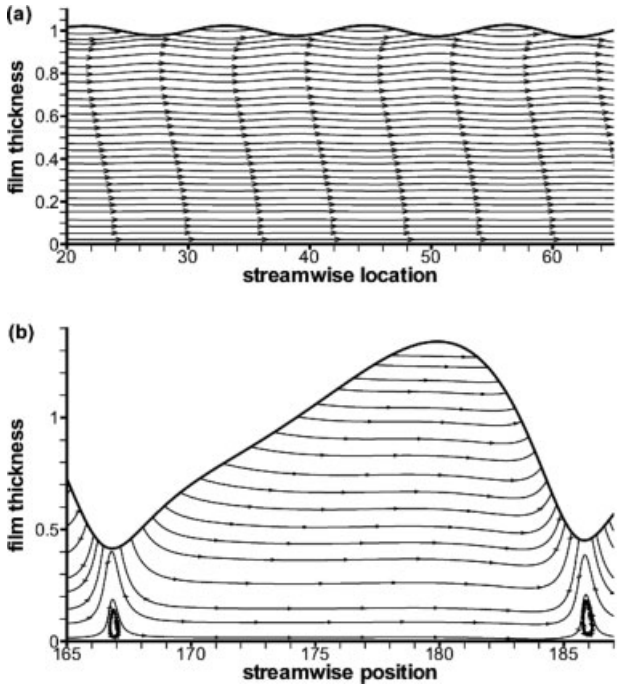

Figure 12. Instantaneous streamlines for waves with intermediate forcing frequencies, calculated at a frame of reference fixed at the wall.

the crest of the wave. The dimensionless frequency of 0.1 is between the frequencies of Figures 11a, b and help us understand the development of the open roll.

The flow field in Figure 12a consists of streamlines that extend from the entrance of the flow field up to the exit and corresponds to the forcing frequency of 0.2. For the given Kapitza and Weber values, this frequency is close to and slightly below the neutral frequency defined by the Orr-Sommerfeld equations. As discussed earlier, the wave velocity in this case exceeds the streamwise velocity at the crest and hence a circulation cannot be seen by an observer moving with the wave. The influence of the waves is confined in a small region near the free surface.

By inspecting the flow field of Figure 12b, we observe the existence of a roll structure in the instantaneous flow field in analogy to the rolls that occur in the Poiseuille-Bénard flow.[27] This roll appears when two hyperbolic and an elliptic point are generated at a critical wave amplitude. As the wave amplitude increases, the hyperbolic points remain on the wall (but the separation between them increases) while the elliptic point moves away from the wall and inside the film. The streamline connecting the two hyperbolic points separates the roll at the wall from the rest of the fluid. The wall shear stress is negative between these two hyperbolic points. Because of the magnitude of the wave minimum, the roll is confined in the liquid film. Every point of the free surface moves in the direction of gravity. This flow field represents the intermediate case of the flow fields in Figures 11a, b. It should be noted that the frequency range for the existence of rolls in Figure 13b is very narrow. It may be in the region $0.105 < f < 0.98$.

Figure 13b shows in more detail how the roll of Figure 12b looks like and how it transforms to an open roll as the forcing frequency increases and the flow rate becomes negative up to the free surface. The open roll in Figure 13a is representative for the roll structures in Figures 11b, c. The flow pattern in Figure 13b is a familiar one, as the roll has two hyperbolic points at the wall and an elliptic point in its center. The novelty is the fact that this kind of rolls have been known so far in flows with temperature gradients. They are detected for vertically falling isothermal films for the first time in this work.

The flow pattern in Figure 13a is a flow situation that we encounter for the first time. It represents a straightforward growth of the roll of Figure 13b. As the roll touches the free surface and the free surface velocity becomes negative, the roll is forced to "open," in a simplistic way of describing what happens, that is why we term the flow pattern of Figure 13a as "open roll." The fact of the matter is that the two hyperbolic points at the wall are still there in Figure 13a as in the conventional roll of Figure 12b. The elliptic point of the roll moves to the free surface in Figure 13a. We also have a source (A) and a sink (B) point at the free surface that connect to the hyperbolic points on the wall and this new flow structure satisfies the criterion of mass conservation. We note that whenever an open roll such as the one shown in Figure 13a exists, the pathlines of the fluid particles on the free surface also have cycloid type loops as shown in Figure 10b. Thus, in this case even the fluid elements at the free surface move forward and backward!

By summarizing the results in Figures 11–13, we observe how the instantaneous flow field of vertical film flows develops with decreasing magnitude of the forcing frequency or increasing wave amplitude. At high forcing frequencies or small wave amplitudes (Figure 12a), the wave velocity exceeds that of any fluid element in the film and the influence of waves is confined to a small region near the free surface. In this case, the waves have certainly no influence near the wall region. As the wave amplitude increases, the velocity at the crest exceeds that of the wave and each wave traps a certain amount of fluid. For low Ka fluids, this trapping may occur before flow reversal near the wall. Further increase in the wave magnitude, enhances both phenomena underneath the minimum of the wave and below its crest, so that rolls are formed below the minimum (Figure 13b). Finally, the rolls grow all the way up to the free surface and the confined streamlines are curved down to the wall, so that the flow field is divided into regions of down flow interrupted by short regions of up flows (Figures 11b, c).

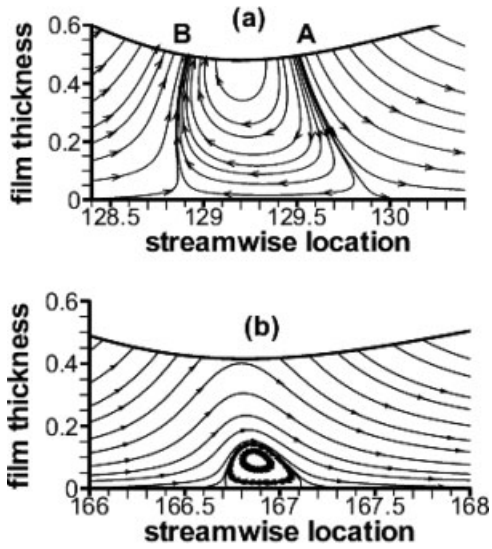

Figure 13. Details of the rolls in Figures 11 and 12.

In other words, to arrive at the flow patterns of Figures 11b, c, which represent the most disturbed flow fields from the familiar Nusselt solution, the disturbance of the initially parallel streamlines of the Nusselt flow starts both from the top of the crest to the direction of the wall and from the wall to the direction of the free surface. That is, the originally parallel streamlines to the wall deviate due to perturbations that start from two opposite directions, which are associated with the maximum and the minimum of the wave.

The present analysis detected the existence of rolls and negative flow regions for this particular flow. These phenomena are much more difficult to identify had the flow field been analyzed in the conventional traveling wave coordinate system. It should be noted though, that in both reference frames it is possible to explain how transfer rates are enhanced by looking at the gradient of the flow field.

Wave Modulation and Oscillatory Rolls in the Experiments of Kapitza and Kapitza (1949)

The analysis of the experiments of Alekseenko et al. intrigued us to look at the historical experiments of Kapitza

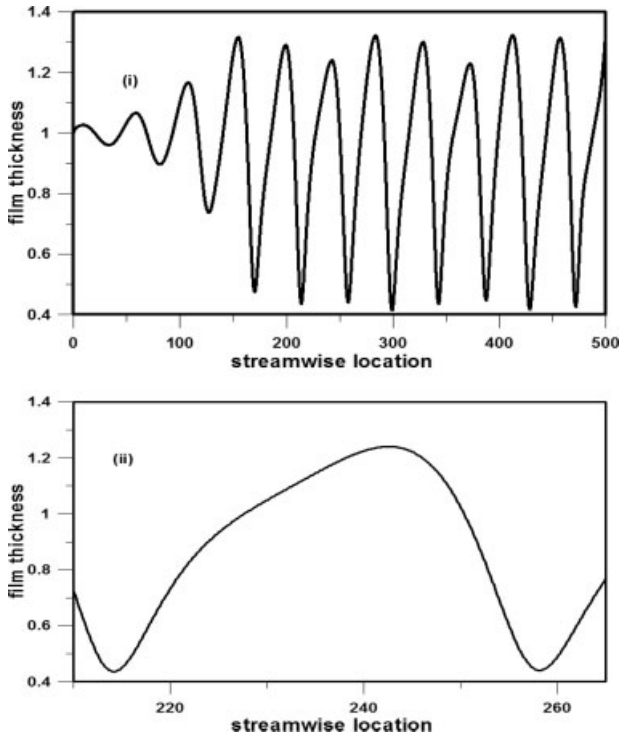

Figure 14. Wave evolution and single wave for Kapitza and Kapitza's experiment.[16]

and Kapitza[16] from the point of view of the existence of flow reversal, roll formation and negative velocity all the way up to the free surface. After all, Kapitza observed a creeping upward motion of liquid helium along the walls of capillaries while studying the heat transfer of this fluid at very low temperatures.[28] This behavior was explained with the fact that liquid helium has almost zero viscosity at these conditions and Kapitza invented the term superfluidity for this phenomenon.

For this purpose, we chose the conditions published in the work of Gao et al.[4] The Weber number is 33.38, the Reynolds number is 20.1, the Kapitza number is 3449.3, and the pulsing frequency is 0.0457. The computational domain is 500 dimensionless Nusselt film thicknesses long and it is tesselated in 10 elements in the y-direction and 10 elements per dimensionless Nusselt film thickness in the x-direction. The amplitude of the pulsation was 5%.

The fully developed waves are shown in Figure 14 along with a single wave. The dimensionless time is 510 units. The shape of the single wave has a similar form to the well known shadow profiles published in the original work of Kapitza and Kapitza,[16] that have been reproduced many times numerically over the last 25 years. What is still unknown though is how the value of the shear stress at the wall changes as a function of time at a fixed point. This is addressed in this work and the results are shown in Figure 15a.

The signal of the shear stress is a periodic one as expected, due to the periodic nature of the flow. However, a change of sign is observed in the shear stress, which suggests flow reversal and roll formation. In the same Figure, the corresponding free surface position of the wave is depicted along with the magnitude of the free surface velocity. The change of sign in the shear stress coincides with the minimum value of the wave amplitude and with a negative value of the free surface velocity. The velocity profiles in the flow reversal region are similar to the ones shown in Figures 4 and 7.

Although these observations are analogous to the analysis of Alekseenko et al.'s experiments, Kapitza's experiment has an additional attribute, which is depicted in Figure 15b. In this Figure, we plot the magnitude of shear stress, free surface minimum and free surface velocity of the first minimum point in Figure 14 where a negative shear stress is observed ($x = 215$) as a function of time. That is, we follow how the value of shear stress, free surface velocity, and amplitude changes with time as the wave moves along the wall. By inspecting Figure 14 closely, we observe that both the minimum and the maximum amplitude of the fully developed wave are not constant, but vary about 0.15 units for the maximum and 0.05 units for the minimum. This change has a major influence in the value of shear stress along the wall and the magnitude of the free surface velocity.

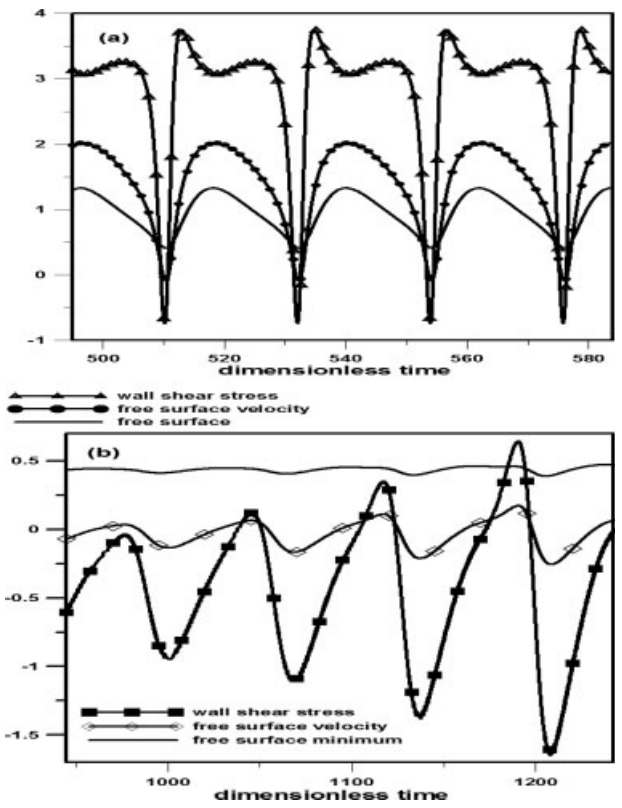

Figure 15. (a) Shear stress as a function of time at a fixed point of the wall for the wave evolution of Figure 14; (b) shear stress, free surface minimum and free surface velocity for the wave minimum at $x = 215$ for the wave evolution of Figure 14.

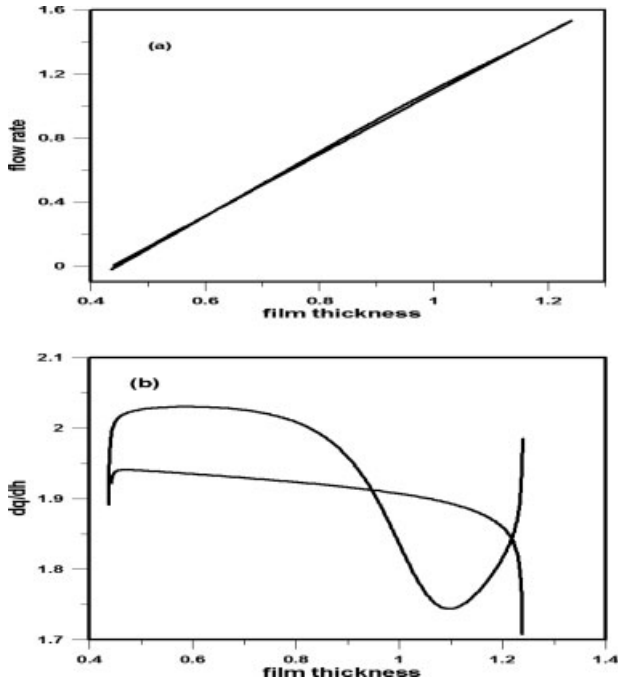

Figure 16. (a) Flow rate vs. film thickness curve for Kapitza's experiment;[16] (b) change of rate of flow rate wrt streamwise location vs film thickness for Kapitza's experiment.[16]

It is shown in Figure 15b, that there is a steady growth in the shear stress as the flow proceeds downstream. However, the small changes in the amplitude of the wave cause oscillations in the shear stress along the wall from negative to positive values, which implies that the roll grows and disappears with the flow. The change in the magnitude of the free surface velocity is in a direct relation to the change in the value of the shear stress. When the shear stress has a negative value, the free surface velocity is negative and the fluid moves locally upward although the film flows vertically downward. When the shear stress has a positive value, the free surface velocity is positive, the roll disappears and the fluid moves locally downward. The value of the minimum amplitude of the wave is also plotted in the same Figure. Although, the change in the amplitude is very small, of the order of 5%, the change in the shear stress and the free surface velocity is unexpectedly very high.

The oscillating nature of the flow field underneath the waves and the unsteady motion of the wave is further confirmed in Figure 16 where we have shown the local flow rate versus film thickness curve and the slope of this curve (which is the wave celerity) versus film thickness. As explained earlier, the wave celerity is not constant in this case, and varies between the values 1.71 and 2.03 [Remark: These results reported here for the first time are helpful in understanding the wavy film behavior for high Kapitza numbers. We have found that these oscillatory flows also occur for the case of Alekseenko et al.'s experiments in a much smaller range of forcing frequencies].

The instantaneous flow field for the wave in Figure 14b is shown in Figure 17a. The streamlines between the two wave minima are again confined by two rolls. The roll on the left has grown all the way up to the free surface and it has transformed to an *open roll*. The roll to the right is still confined in the interior of the film. The whole flow proceeds at each instant of time divided in regions of down flows interrupted by small regions of up flows as is the case with the waves produced by Alekseenko et al.[2] The only difference to the previous experiments is that the region of down flow may extend up to two wave lengths as opposed to one wave length in the previous subsection, due to the oscillating nature of the rolls which grow and disappear constantly. Such oscillating rolls have not been previously reported for isothermal flows neither for this flow nor for other cases.

Details on the growth of these rolls are given in Figures 17b, c, where the flow field under the minima of the wave of Figure 17a is magnified. The only difference between the results of this Figure with Figure 13 is that the roll of Figure 17b oscillates in time and space, so that it may disappear (case not shown), grow (Figure 17c) and expand up to the free surface (Figure 17b). The existence of these *oscillating rolls* in the instantaneous flow field of the film with high

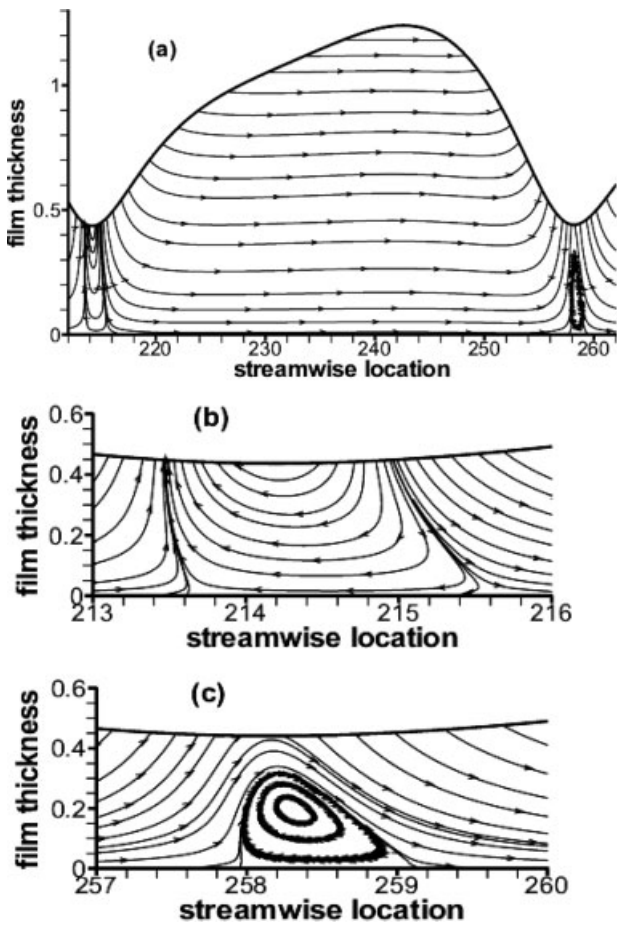

Figure 17. Instantaneous streamlines for the wave in Figure 14(ii), calculated at a frame of reference fixed at the wall along with details of the rolls that appear under the minima of the wave.

Kapitza number is expected to enhance heat and mass transfer even further than in the previous analysis of Alekseenko et al.'s experiments.

It is not clear if Kapitza knew the existence of oscillating shear stress at the wall in his 1949 experiments, since he gives no information about that in his paper. It is also not clear whether he made these experiments, in order to check if Newtonian fluids with finite viscosity exhibit a locally upward motion while flowing in the direction of gravity, a phenomenon he first observed with liquid helium. However, in his water experiments at room temperature, there is a locally confined upward motion of liquid that is caused by a roll which is formed at the wall and develops all the way up to the free surface, where it degenerates to an "open roll." Our work sheds light to that side of Kapitza's experiment for the first time.

Before closing this section, we state a final new result of our computations for the high Ka case. For Ka = 1000, We = 5 and a forcing frequency of 0.02 we found as many as five capillary ripples in front of the main hump of the wave. Examination of the vorticity profile along the wall showed four sign reversals indicating that there are four regions with negative wall shear stress. Examination of the instantaneous streamlines showed that the velocity profile is negative up to the free surface in the first three regions while the roll has not reached the surface in the fourth capillary ripple.

Summary and Discussion

The main contributions of this work may be summarized as follows: (a) elucidation of the velocity profiles, flow structure and quantities such as the local flow rate and wall shear stress in the wavy film corresponding to the experiments of Alekseenko et al. and Kapitza and Kapitza, (b) elucidation of the flow structure in the wavy film in the stationary as well as moving frames of reference through plotting of instantaneous streamlines and pathlines, (c) discovery of cellular stationary and oscillatory patterns in the instantaneous flow field of the film, (d) use of the linear relationship between flow rate and film thickness for a wave to determine whether or not it is moving with a constant velocity, and (e) physical interpretation of the regions in which wall shear stress is negative, i.e., in these regions, the wall to film transport is enhanced (while the traditional explanation using traveling wave coordinate system deals with the enhancement of transport at the gas–liquid interface).

We now discuss briefly some (but most certainly not all) of the unresolved issues related to film flows. First, the calculations presented here deal only with 2D flows. It is known experimentally that the 2D solitary waves can become unstable and lead to 3D waves. It is not clear how this instability relates to the change in the flow structure underneath these waves. Second, the present calculations are confined to the viscocapillary regime ($We \geq 1$) but the case of most practical interest is the inertial regime ($We < 1$). Experimentally, it is known that for high Kapitza fluids like water, the wave amplitude in the inertial regime can be as large as 10 times the mean film thickness. Further, these large amplitude waves can develop singularities during their evolution and lead to droplet formation. Equivalently, for any fixed Ka (fluid properties), there exists a critical flow rate ($We = We_c$) above which ($We < We_c$) there is no bounded solution to the film flow equations. Finally, it is not clear how the shear instabilities (Tollman-Schlichting) that appear in the film in the inertial regime interact with the cellular structures generated in the viscocapillary regime studied here. The calculation of the flow structure in the film for these cases is challenging even for the 2D case!

Acknowledgments

The authors thank professor Fazle Hussain for many helpful discussions and for suggesting to look at vorticity profiles in the film. All computations have been performed using the Beowulf cluster of the High Performance Center for Scientific Computing of the University of Houston. Author N.A.M. has been partially supported by the research grant ARCHIMEDES I of the Hellenic Ministry of Education. The work of V. Balakotaiah was supported by the University of Houston through a Moores Professorship.

Literature Cited

1. Alekseenko SV, Nakoryakov VY, Pokusaev BG. Wave formation on a vertical falling liquid film. *AIChE J*. 1985;31:1446–1460.
2. Alekseenko SV, Nakoryakov VE, Pokusaev BG. *Wave Flow of Liquid Films*. New York: Begell House, 1994.
3. Chang HC, Demekhin EA. *Complex Wave Dynamics on Thin Films*. Amsterdam: Elsevier Science, 2002.
4. Gao D, Morley NB, Dhir V. Numerical simulation of wavy falling film flow using VOF method. *J Comp Physics*. 2003;192:624–642.
5. Nosoko T, Miyara A. The evolution and subsequent dynamics of waves on a vertically falling liquid film. *Phys Fluids*. 2004;16:1118–1126.
6. Scheid B, Ruyer-Quil C, Manneville P. Wave patterns in film flows: modelling and three-dimensional waves. *J Fluid Mech*. 2006;562:183–222.
7. Tihon J, Serifi K, Argyriadi K, Bontozoglou V. Solitary waves on inclined films: their characteristics and the effects on wall shear stress. *Exp Fluids*. 2006;41:79–89.
8. Mudunuri R, Balakotaiah V. Solitary waves on thin falling films in the very low forcing frequency limit. *AIChE J*. 2006;52:3995–4003.
9. Wasden FK, Dukler AE. Insights into the hydrodynamics of free falling wavy films. *AIChE J*. 1989;35:187–195.
10. Miyara A. Numerical simulation of wavy film flowing down on a vertical wall and an inclined wall. *Int J Therm Sci*. 2000;39:1015–1027.
11. Yu LQ, Wasden FK, Dukler AE, Balakotaiah V. Nonlinear evolution of waves on falling films at high Reynolds numbers. *Phys Fluids*. 1995;7:1886–1902.
12. Ruyer-Quil C, Manneville P. Improved modeling of flows down inclined planes. *Eur Phys J*. 2000;B15:357–369.
13. Massot C, Irani F, Lightfoot EN. Modified description of wave motion in a falling film. *AIChE J*. 1966;12:445–455.
14. Malamataris NA, Vlachogiannis M, Bontozoglou V. Solitary waves on inclined films: flow structure and binary interactions. *Phys Fluids*. 2002;14:1082–1094.
15. Tihon J, Tovchigrechko V, Sobolik V, Wein O. Electrodiffusion detection of the near-wall flow reversal in liquid films at the regime of solitary waves. *J App Electrochem*. 2003;33:577–587.
16. Kapitza PL, Kapitza SP. Wave flow in thin layers of a viscous fluid. In: ter Haar D, editor. *Collected Papers of P.L. Kapitza*. New York: The Macmillan Company, 1964:Vol. II:662.
17. Malamataris N, Papanastasiou TC. Unsteady free surface flows on truncated domains. *Ind Eng Chem Res*. 1991;30:2211–2219.
18. Malamataris NA, Bontozoglou V. Computer aided analysis of viscous film flow along an inclined wavy wall. *J Comp Physics*. 1999;154:372–392.
19. Ho LW, Patera AT. A Legendre spectral element method for simulation of unsteady incompressible viscous free surface flows. *Comput Methods Appl Mech Eng*. 1990;80:355–366.
20. Salamon TR, Armstrong RC, Brown RA. Traveling waves on vertical films: numerical analysis using the finite element method. *Phys Fluids*. 1994;6:2202–2220.

21. Ramaswamy B, Chippada S, Joo SW. A full-scale numerical study of interfacial instabilities in thin-film flows. *J Fluid Mech*. 1996; 325:163–194.
22. Kunugi T, Kino C. DNS of falling film structure and heat transfer via MARS method. *Comput Struct*. 2005;83:455–462.
23. Panga MKR, Balakotaiah V. Low dimensional models for vertically falling viscous films. *Phys Rev Lett*. 2003;90:154501.
24. Meza C, Balakotaiah V. Modeling and experimental studies of large amplitude waves on vertically falling films. *Chem Eng Sci*. in press 2008.
25. Liu J, Gollub JP. Onset of spatially chaotic waves on flowing films. *Phys Rev Lett*. 1993;70:2289–2292.
26. Liu J, Gollub JP. Solitary wave dynamics of film flows. *Phys Fluids*. 1994;7:1702–1792.
27. Xu C, Lin Y. A numerical comparison of outflow boundary conditions for spectral element simulations of incompressible flows. *Comm Comp Phys*. 2007;2:477–500.
28. Kapitza PL. The study of heat transfer in helium II. In: ter Haar D, editor. *Collected Papers of P.L. Kapitza*. New York: The Macmillan Company, 1964:Vol. II:681.

Manuscript received May 21, 2007, and revision received Mar. 12, 2008.